

Dense molecular globulettes and the dust arc toward the runaway O star AE Aurigae (HD 34078)^{★,★★}

P. Gratier^{1,2,3}, J. Pety^{1,4}, P. Boissé⁵, S. Cabrit⁴, P. Lesaffre^{4,6}, M. Gerin⁴, and G. Pineau des Forêts^{7,4}

¹ IRAM, 300 rue de la Piscine, 38406 Saint-Martin d'Hères, France
e-mail: [gratier,pety]@iram.fr

² Univ. Bordeaux, LAB, UMR 5804, 33270 Floirac, France

³ CNRS, LAB, UMR 5804, 33270 Floirac, France

⁴ LERMA, UMR 8112, CNRS, Observatoire de Paris, ENS, UPMC, UCP, 61 avenue de l'Observatoire, 75014 Paris, France

⁵ IAP, UMR 7095 CNRS and Sorbonne Universités, UPMC Univ Paris 06, 98bis boulevard Arago, 75014 Paris, France

⁶ VATLY, Institute for Nuclear Science and Technology, 179 Hoang Quoc Viet, Cau Giay, Ha Noi, Viet Nam

⁷ IAS, UMR 8617, CNRS, Bâtiment 121, Université Paris Sud 11, 91405 Orsay, France

Received 19 January 2014 / Accepted 25 March 2014

ABSTRACT

Context. Some runaway stars are known to display IR arc-like structures around them, resulting from their interaction with surrounding interstellar material. The properties of these features as well as the processes involved in their formation are still poorly understood.

Aims. We aim to understand the physical mechanisms that shape the dust arc observed near the runaway O-star AE Aur (HD 34078).

Methods. We obtained and analyzed a high spatial resolution (4.4'') map of the ¹²CO(1–0) emission that is centered on HD 34078, and that combines data from both the IRAM interferometer and 30 m single-dish antenna.

Results. One third of the 30 m flux mainly originates from two small (no larger than 5'' × 10'' or 0.013 × 0.026 pc), and bright (1 and 3 K peak temperatures) CO globulettes. The line of sight toward HD 34078 intersects the outer part of one of the globulettes, which accounts for both the properties of diffuse UV light observed in the field and the numerous molecular absorption lines detected in HD 34078's spectra, including those from highly excited H₂. Their modeled distance from the star (0.2 pc) is compatible with the fact that they lie on the 3D paraboloid, which fits the arc detected in the 24 μm *Spitzer* image. Four other compact CO globulettes are detected in the mapped area, all lying close to the rim of this paraboloid. These globulettes have a high density and linewidth, and are strongly pressure-confined or transient.

Conclusions. The presence of molecular globulettes at such a close distance from an O star is unexpected, and probably related to the high proper motion of HD 34078. Indeed, the good spatial correlation between the CO globulettes and the IR arc suggests that they result from the interaction of the radiation and wind emitted by HD 34078 with the ambient gas. However, the details of this interaction remain unclear. A wind mass-loss rate significantly larger than the value inferred from UV lines is favored by the large IR arc size, but does not easily explain the low velocity of the CO globulettes. The effect of radiation pressure on dust grains also meets several issues in explaining the observations. Further observational and theoretical work is needed to fully elucidate the processes shaping the gas and dust in bow shocks around runaway O stars.

Key words. circumstellar matter – stars: individual: HD 34078 – HII regions – stars: winds, outflows

1. Introduction

The interstellar medium (ISM) was discovered in 1907 by studying atomic absorption lines (from NaI and CaII) seen in the visible spectrum of bright stars. The first interstellar molecules (CN, CH, and CH⁺) were also detected in the same way in the years 1937–1940. In the seventies, the Copernicus satellite systematically studied H₂ ultraviolet (UV) absorption lines to investigate the properties of diffuse interstellar gas with low visual extinction ($A_v \leq 1$ mag), and this powerful method is still largely used today (cf. Far Ultraviolet Spectroscopic Explorer (FUSE), *Hubble* Space Telescope/Space Telescope Imaging Spectrograph

(HST/STIS), and *Hubble* Space Telescope/Cosmic Origins Spectrograph (HST/COS) programs). The gas in diffuse clouds is mainly neutral, warm (typically 80 K), and (usually) of low density (100–500 cm⁻³). Such regions correspond to the transition from atomic to molecular hydrogen, where carbon is still mostly ionised or neutral, with $N(\text{CO}) < \text{a few } 10^{16} \text{ cm}^{-2}$, and $N(\text{C}) \sim 3 \times 10^{17} \text{ cm}^{-2}$.

In this framework, the foreground absorption against the O9.5 star HD 34078 stands out for its peculiar properties. The star HD 34078 was ejected about 2.5 Myr ago from the Orion region (Blaauw & Morgan 1953; Bagnuolo et al. 2001) and is now the fastest runaway star in the local ISM, with a velocity of $V_\star \sim 150 \text{ km s}^{-1}$ (Tetzlaff et al. 2011). The line of sight toward HD 34078 should thus offer a means to detect small scale (5–50 au) density or abundance variations in the diffuse ISM in only a few decades. However, as absorption line studies progressed, it was realized that this line of sight exhibits peculiar properties compared to the usual diffuse ISM on other lines of sight. Very abundant CH and CH⁺ is measured with some

* Based on observations carried out with the IRAM Plateau de Bure Interferometer. IRAM is supported by INSU/CNRS (France), MPG (Germany), and IGN (Spain).

** PdeB map in FITS format is only available at the CDS via anonymous ftp to cdsarc.u-strasbg.fr (130.79.128.5) or via <http://cdsarc.u-strasbg.fr/viz-bin/qcat?J/A+A/570/A71>

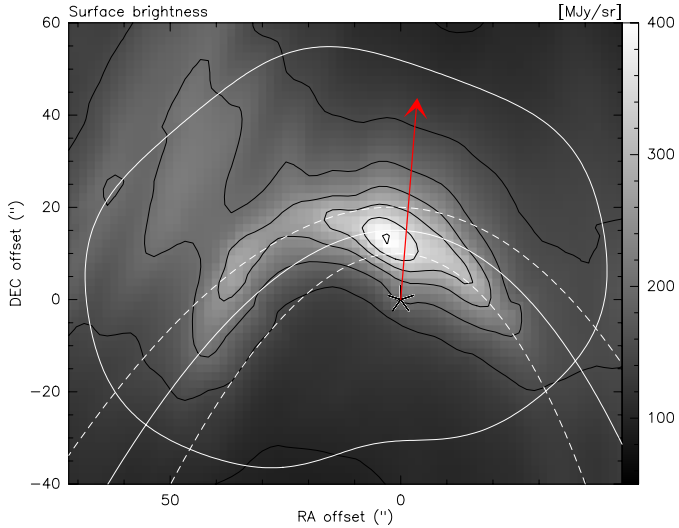


Fig. 1. *Spitzer* $24\mu\text{m}$ image toward HD 34078, from (France et al. 2007). Contours are equally spaced every 50 MJy/sr, starting from 100 MJy/sr. Offsets are measured from the star position, displayed as a black star. The red arrow represents the star on-sky proper motion for the next 1000 years. The solid open white curve displays a parabola pointing in this direction, with its focus at the star and a projected star-apex distance $R_{\text{obs}} = 15''$ (see Appendix A for a description of projection effects in a paraboloid). The two dashed curves correspond to variations of R_{obs} by $\pm 5''$. The closed white contour corresponds to the region mapped with the PdBI interferometer. The right ascension axis increases toward the left.

time variability (Rollinde et al. 2003). The direct starlight suffers larger reddening than scattered light in the surrounding nebula (France et al. 2004). In addition, UV absorption studies with FUSE reveal an unusually large amount of highly excited H_2 , indicating the unexpected presence of dense ($n_{\text{H}} \approx 10^4 \text{ cm}^{-3}$) and strongly irradiated molecular gas at about 0.2 pc from the star (Boissé et al. 2005). The latter property could be related to the recent interaction of the star with the IC 405 reflection nebula (Herbig 1958). Indeed, the emission of hot dust at $24\mu\text{m}$ imaged with *Spitzer*/MIPS clearly delineates a parabolic curve (see Fig. 1), interpreted as the tip of a bow shock resulting from the interaction of fast stellar wind with the preexisting diffuse gas of IC 405 (France et al. 2007).

In order to gain 2D information on the molecular gas structure and kinematics in this bow shock, Boissé et al. (2009) conducted sensitive $^{12}\text{CO}(2-1)$ mapping in a narrow field of view around HD 34078 using the IRAM-30 m telescope at an angular resolution of $12''$. On top of a widespread CO component, brighter emission was detected in a clumpy “filament” peaking slightly below the $24\mu\text{m}$ arc, confirming ongoing interaction between the star and the surrounding cloud. However, the CO velocity field showed a gradient mainly perpendicular to the star-apex axis, instead of mainly along this axis as expected for a steady-state wind bow shock (see, e.g., Wilkin 1996). In addition, Boissé et al. (2009) noted that the apparent distance between the star and the IR arc of $15''$, corresponding to 0.04 pc at the distance of HD 34078 ($\approx 530 \text{ pc}$ assuming $M_V = -4.2$ Herbig 1999), is largely incompatible with the prediction of a stationary bow shock for the wind mass flux derived from UV line analysis (Martins et al. 2005). They then proposed that we might be witnessing the recent birth of the bow shock, or that radiation pressure on grains might play a role in increasing its size. Alternatively, the wind mass flux might have been largely underestimated (as proposed by Gvaramadze et al. 2012,

to explain the IR bow shock size in ζ Oph), or some other under appreciated physical process could be at play.

Distinguishing between these hypotheses is crucial to better understand the processes that govern the interaction between HD 34078 and the surrounding ISM, how they impact the absorbing gas properties on the line of sight, and how they may affect the wind mass flux determinations from IR bow shock sizes in other runaway O stars. As a step toward this goal, we mapped the bowshaped IR arc around HD 34078 in $^{12}\text{CO}(1-0)$ with the Plateau de Bure Interferometer (PdBI, complemented with IRAM-30 m single-dish data to provide the short-spacings at $\approx 4''$ resolution, comparable to the $24\mu\text{m}$ *Spitzer* image and three times better than the $^{12}\text{CO}(2-1)$ map of Boissé et al. (2009).

The observations and data reduction are presented in Sect. 2. The resulting properties of the detected CO structures are described in Sect. 3. We discuss their implications in Sect. 4. We summarize and conclude in Sect. 5.

2. Observations and data reduction

Table 1 summarizes the interferometric and single-dish observations described in this section.

2.1. Interferometric observations and data reduction

Interferometric observations of HD 34078 were obtained at the Plateau de Bure Interferometer (PdBI) operated by IRAM. We carried out these observations with five antennas in the D configuration (baselines from 24 to 96 meters) in August 2011. We observed a mosaic of 13 pointings that followed a hexagonal compact pattern with closest neighbors separated by half the primary beam. The mosaic thus covers a field of view of $120'' \times 100''$. We used the D configuration of the array, yielding a typical synthesized angular resolution of $4.4''$. The observations include about 19 h of telescope time. The on-source time scaled to a six antenna array is 8.5 h. Three correlator windows of 40 MHz were concatenated to form a continuous bandwidth of 300 km s^{-1} centered on the $^{12}\text{CO}(1-0)$ rest frequency (115.271 GHz) at a resolution of 0.2 km s^{-1} . During the observations, the typical precipitable water vapor amounted to 4–8 mm and the typical system temperature was 200 K. The median noise level achieved over the mosaic is 0.14 K (T_{mb}) in channels of 0.4 km s^{-1} width.

We used the standard algorithms implemented in the GILDAS/CLIC software to calibrate the PdBI data. The radio-frequency bandpass was calibrated by observing the bright (9 Jy) quasar 3C454.3. We calibrated phase and amplitude temporal variations by fitting spline polynomials through regular measurements of two nearby ($<12^\circ$) quasars (J0418+380 and 0548+398). The PdBI secondary flux calibrator MWC 349 was observed once during every track, which allowed us to derive the flux scale of the interferometric data. The absolute flux accuracy is $\sim 10\%$.

2.2. Single dish mapping observations and data reduction

A multiplicative interferometer filters out the low spatial frequencies, i.e., spatially extended emission. We thus observed the same region with the IRAM-30 m single dish telescope to recover the low spatial frequency (“short- and zero-spacing”) information filtered out by the PdBI. We describe here the observing strategy and the calibration, baselining, and gridding methods we used to obtain single-dish data whose quality matches the interferometric data.

Table 1. Observation parameters.

Molecule	Transition	Frequency (GHz)	Instr.	Config.	Beam (")	PA (deg)	Vel. res. (km s ⁻¹)	Int. Time ^a (hr)	Tsys (K)	Noise ^b (mK)	Obs. date	
¹² CO	<i>J</i> = (1–0)	115.27120	PdBI	5D	5.1 × 3.8	139	0.2	8.5/19	200	140	Aug. 2011	
Molecule	Transition	Frequency (GHz)	Instr.	#pol	<i>F</i> _{eff}	<i>B</i> _{eff}	Res. (")	Res. (km s ⁻¹)	Int. Time (hr)	Tsys (K)	Noise ^b (mK)	Obs. date
¹² CO	<i>J</i> = (2–1)	230.53800	30 m/E2	2	0.91	0.59	11.2	0.4	7.1/20	460	140	May 2012
¹² CO	<i>J</i> = (1–0)	115.27120	30 m/E0	2	0.95	0.78	22.5	0.4	7.1/20	230	65	May 2012

Notes. The projection center for the all the observations is $\alpha_{2000} = 05^{\text{h}}16^{\text{m}}19.143^{\text{s}}$, $\delta_{2000} = 34^{\circ}18'52.34''$ the position of HD 34078. ^(a) listed as on-source time/telescope time ^(b) evaluated at the mosaic phase center (the noise steeply increases at the mosaic edges after correction for primary beam attenuation, see top panel of Fig. 3).

The single dish observations were taken at the IRAM-30 m telescope in May 2012 during 20 h of average summer time (9 mm median water vapor, $T_{\text{sys}} \sim 230$ K at 3 mm and $T_{\text{sys}} \sim 460$ K at 1 mm). We observed simultaneously at 3 and 1 mm with a combination of the EMIR receivers and the Fourier transform spectrometers, which yields a bandwidth of 3.6 GHz per polarization at a frequency resolution of 49 kHz. This allowed us to measure ¹²CO(1–0), ¹²CO(2–1), ¹³CO(1–0), and half of the CN(1–0) hyperfine lines.

We used the on-the-fly scanning strategy with a dump time of 0.4 s and a scanning speed of 5.5"/s to ensure a sampling of five dumps per beam at the 11" resolution of the ¹²CO(2–1) line. The 300" × 250" map was covered using successive orthogonal scans along the RA and Dec axes. The separation between two successive rasters was 4.3" ($\sim \lambda/D$) to ensure Nyquist sampling. A common off reference position located at offsets (−400", −200") was observed for 10 s every 40 to 50 s. The calibration parameters (including the system temperature) were measured every 20 min using the hot/cold/sky load method. The pointing was checked every hour and the focus every 4 h. The typical IRAM-30 m position accuracy is $\sim 2''$.

Data reduction was carried out using the GILDAS/CLASS software. A 20 MHz-wide subset of the spectra was first extracted around each line’s rest frequency. We then computed the experimental noise by subtracting a zeroth order baseline from every spectrum. A systematic comparison of this noise value with the theoretical noise computed from the system temperature, the integration time, and the channel width, allowed us to filter out outlier spectra. This amounted to a few tens over the 212 700 spectra of the full dataset. The spectra were then gridded to a data cube through a convolution with a Gaussian kernel of $FWHM \sim 1/3$ of the telescope beamwidth. Finally, we fitted another baseline of order 3 through each spectrum of the cube. The two steps of baselining excluded a velocity range of 0 to 10 km s⁻¹ LSR, where the signal resides.

2.3. Joint imaging and deconvolution of the interferometric and single-dish data

Following Rodríguez-Fernández et al. (2008), the GILDAS/MAPPING software and the single-dish map from the IRAM-30 m were used to create the short-spacing visibilities not sampled by the Plateau de Bure interferometer. In short, the maps were deconvolved from the IRAM-30 m beam in the Fourier plane before multiplying by the PdBI primary beam in the image plane. After a last Fourier transform, pseudo-visibilities were sampled between 0 and 15 m (the diameter of the PdBI antenna). These visibilities were then merged with

the interferometric observations. Each mosaic field was imaged and a dirty mosaic was built combining those fields in the following optimal way in terms of signal-to-noise ratio (Pety & Rodríguez-Fernández 2010) :

$$J(\alpha, \delta) = \sum_i \frac{B_i(\alpha, \delta)}{\sigma_i^2} F_i(\alpha, \delta) \left/ \sum_i \frac{B_i(\alpha, \delta)^2}{\sigma_i^2} \right.$$

In this equation, $J(\alpha, \delta)$ is the brightness distribution in the dirty mosaic image, B_i are the response functions of the primary antenna beams, F_i are the brightness distributions of the individual dirty maps, and σ_i are the corresponding noise values. As can be seen in this equation, the dirty intensity distribution is corrected for primary beam attenuation, which induces a spatially inhomogeneous noise level. In particular, noise strongly increases near the edges of the field of view. To limit this effect, both the primary beams used in the above formula and the resulting dirty mosaics are truncated. The standard level of truncation is set at 20% of the maximum in MAPPING. The dirty image was deconvolved using the standard Högbom CLEAN algorithm. The resulting data cube was then scaled from Jy/beam to T_{mb} temperature scale using the synthesized beam size (see Table 1).

3. Observational results

Figure 2 compares the spatial distributions of the ¹²CO(1–0) integrated emission at the resolutions of the IRAM-30 m and PdBI instruments. The IRAM-30 m map was masked to display exactly the same field of view as the hybrid (PdBI + IRAM-30 m) synthesis map. The noise is nonuniform in both maps. A 50"-square patch centered on the star position was observed longer at the IRAM-30 m to improve the signal-to-noise ratio in this region. In addition, the noise naturally increases at the edges of the mosaic because of the correction of the interferometer primary beam attenuation.

Two unresolved bright “globules” clearly pop up at the resolution of the IRAM-30 m. The brightest “globule”, located to the southeast of the star, is only partly included inside the observed field of view. We thus saturate the corresponding region in the color scale of Fig. 2 to outline the structure of the second bright emitting region close to the star, previously studied with the IRAM-30 m by Boissé et al. (2009). We find that, at the higher resolution of the hybrid map, this “globule” clearly breaks up into two bright (up to 3 K km s⁻¹) globulettes denoted as #1 and #2 in Fig. 2, and peaking less than 10" on either side from the star sightline. They are clearly elongated, with a typical length of $\sim 10''$ and a width of $\sim 4''$ – $5''$ (i.e., barely resolved) in the perpendicular direction. In both cases, the elongation is roughly pointing in the direction of the star.

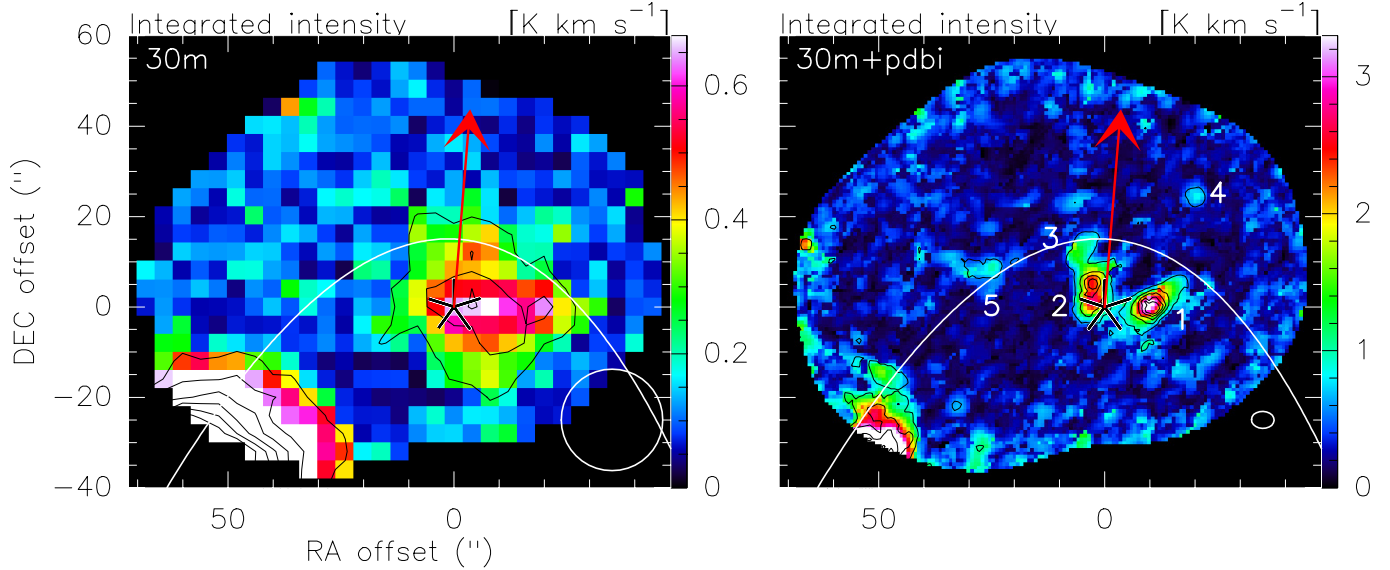


Fig. 2. Spatial distributions of the $^{12}\text{CO}(1-0)$ line integrated intensities. The left/right panels show the data from IRAM-30 m only (at an angular resolution of $22.5''$), and the hybrid synthesis data from PdBI + IRAM-30 m (at an angular resolution of $5.1'' \times 3.8''$ at a position angle of 139°), respectively. The beam shape is drawn as an ellipse in the lower right corner of each panel. Black contours are drawn at 5, 10, 15, 20, 25, and 30σ . Offsets are measured from the star position, denoted by the black star with the red arrow representing the star on-sky motion for the next 1000 years. The parabola adjusted to the $24\mu\text{m}$ arc in Fig. 1 with $R_{\text{obs}} = 15''$ is reproduced here to guide the eye. The numbers 1–5 refer to the globulettes discussed in the text.

Three other globulettes are detected in the hybrid synthesis map with a signal-to-noise ratio larger than 5. These lower brightness ($\lesssim 1 \text{ K km s}^{-1}$) structures, denoted as #3, #4, and #5 in Fig. 2, are smaller, rounder, and projected further from the star than bright globulettes #1 and #2. Interestingly, they all fall close to a parabola (drawn as a white curve in Fig. 2) with its focus at the star and passing through the IR arc ahead of HD 34078. The same is found for the bright globule at the southeastern edge of our field of view. We will further comment on the possible physical link between CO substructures and the IR arc in Sect. 4.

Figure 3 displays the spatial distributions of the noise, peak temperature, line integrated intensities, and centroid velocities of the hybrid synthesis CO data. Eastern globulette #1 has a significantly lower peak temperature ($\sim 1 \text{ K}$) than western globulette #2 ($\sim 3 \text{ K}$). The eastern/western globulettes have a typical LSR velocity of ~ 5.5 and 7.4 km s^{-1} , respectively. These velocities approximately correspond to the two velocity peaks in the IRAM-30 m $^{12}\text{CO}(1-0)$ and $^{12}\text{CO}(2-1)$ spectra obtained less than $3''$ from the star sightline¹, which are shown in the top panel of Fig. 5. Our higher resolution dataset thus reveals that the double-peaked shape of IRAM-30 m CO spectra close to the star does not result from absorption by foreground gas, but from the beam dilution of two almost distinct globulettes that each contributes to one of the observed CO velocity peaks. The spatial offset between these two globulettes also readily explains the east-west velocity gradient observed at $12''$ resolution with the IRAM-30 m by Boissé et al. (2009).

The bottom left panel of Fig. 4 shows a zoom of the hybrid synthesis data toward substructures #1 and #2. The line of sight toward the star falls right at the edge of eastern globulette #1. In addition, position-velocity diagrams (Fig. 4, upper left and lower right panels) show that western substructure #2 at 7 km s^{-1} has a faint extension to the east, so that the sightline

Table 2. Properties of the two spectral components in the direction of HD 34078 derived from PdBI+30 m data with $4.4''$ angular resolution.

Spectral component	1	2
V_{LSR} (km s^{-1})	4.9 ± 0.1	6.9 ± 0.2
ΔV_{CO} (km s^{-1})	1.3 ± 0.2	0.8 ± 0.7
W_{CO} (K km s^{-1})	1.1 ± 0.3	0.4 ± 0.4
A_v (mag)	0.23 ± 0.06	0.08 ± 0.08

actually intercepts both velocity components. The corresponding $^{12}\text{CO}(1-0)$ emission spectrum toward HD 34078 at a resolution of $4.4''$ is shown in the bottom panel of Fig. 5. Table 2 lists the results of a dual Gaussian fit to this emission spectrum. The two fitted velocity components are in remarkable agreement with the two narrow absorption components at $V_{\text{LSR}} \sim 5$ and $V_{\text{LSR}} \sim 7 \text{ km s}^{-1}$ identified in both CH and CH⁺ from high-resolution ($\text{FWHM} \approx 2 \text{ km s}^{-1}$) optical spectra (see Figs. 5, 7, and 8 of Rollinde et al. 2003), even though the PdBI lobe probes a wider region than the star pencil beam. This result unambiguously shows that CO(1–0) globulettes #1 and #2 are located in front of the star, and not in its background.

Table 2 also lists the visual extinction of the star that would be contributed by each CO velocity component assuming a standard X_{CO} conversion factor $W_{\text{CO}}/N(\text{H}_2) = 2 \times 10^{20} \text{ cm}^{-2}/(\text{K km s}^{-1})$, and a standard ratio of $N_{\text{H}}/A_v = 1.8 \times 10^{21} \text{ cm}^{-2}$. The sum is $A_v(\text{CO}) = 0.3 \pm 0.1 \text{ mag}$. This is in excellent agreement with expectations. Indeed, the reddening suffered by HD 34078, $E_{B-V} = 0.52$ (France et al. 2004) implies a total visual extinction of $E_{B-V} \times 3.1 = 1.6 \text{ mag}$ (cf. Fitzpatrick & Massa 1990, who find a standard extinction curve toward HD 34078). Out of this, 1.1–1.5 mag comes from atomic HI, whose Ly α and Ly β absorption indicate $N(\text{HI}) = 2\text{--}2.7 \times 10^{21} \text{ cm}^{-2}$ (Shull & van Steenberg 1985; Boissé et al. 2005). This leaves 0.1–0.5 mag of extinction by molecular gas on the line of sight. Therefore, the effective X_{CO} factor in the CO(1–0)

¹ The $^{12}\text{CO}(2-1)$ spectrum is similar to that presented in Boissé et al. (2009), but the $^{12}\text{CO}(1-0)$ is smaller by a factor ~ 2 . This could come from an erroneous conversion from T_{A}^* to T_{mb} in the former paper.

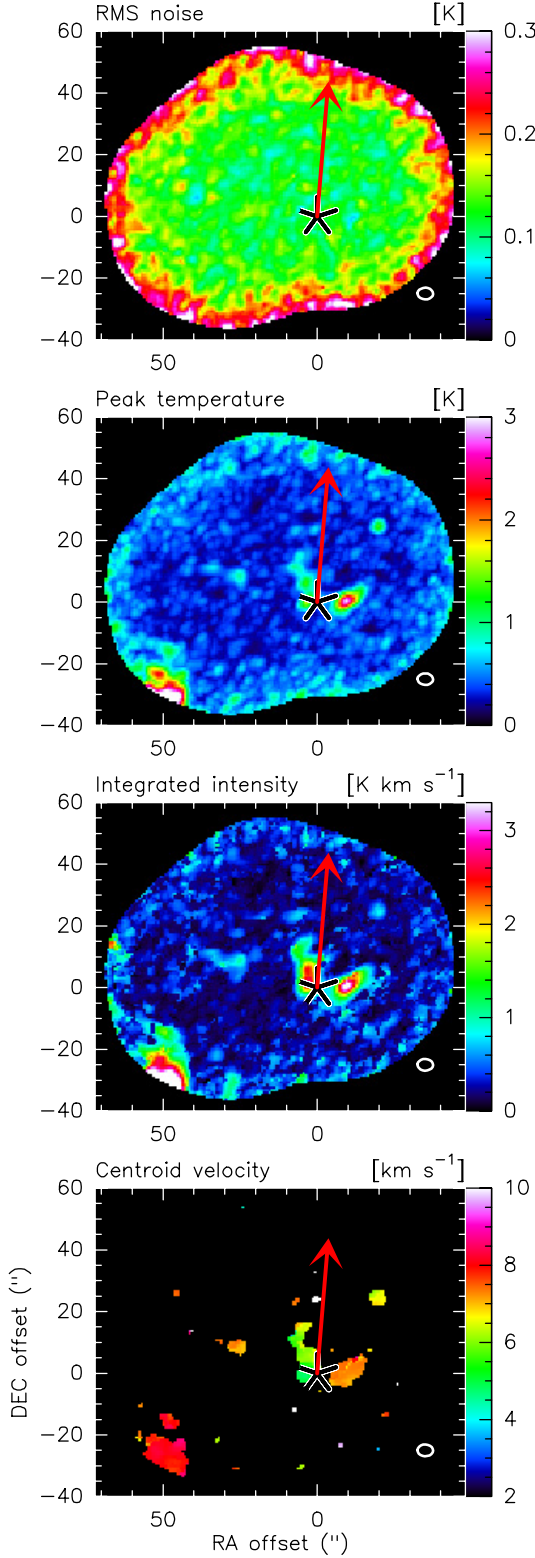


Fig. 3. Maps for the $^{12}\text{CO}(1-0)\text{PdBI}+30$ m data. *From top to bottom* RMS noise, peak temperature, integrated intensity, and centroid velocity. In the last case, only the pixels with a peak signal-to-noise ratio larger than 5 are shown.

emitting gas appears close to standard (within a factor 2) and may be used to infer the globulette masses.

Table 3 lists quantitative information about the five small globulettes. Using standard values for the X_{CO} factor and for $N_{\text{H}}/A_{\text{v}}$, we derived their peak visual extinction from their

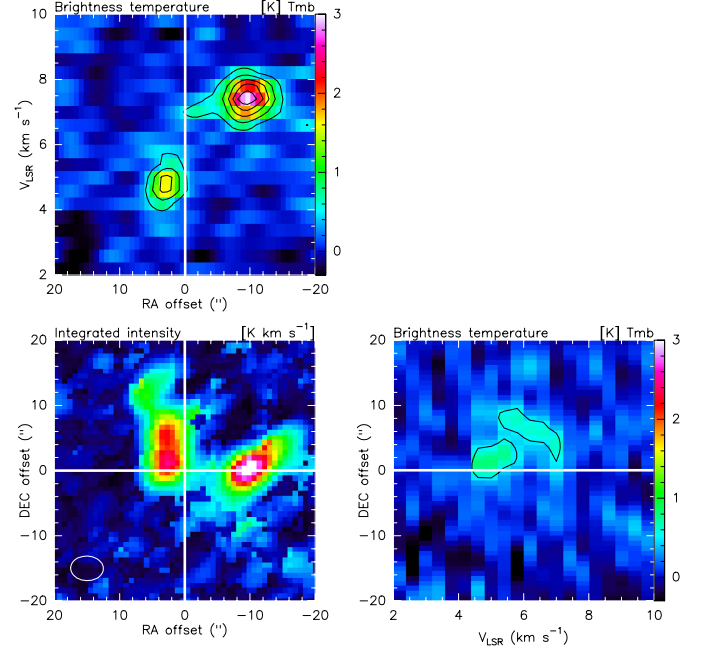


Fig. 4. Position velocity slice along the right ascension (*upper left*) and declination (*lower right*) axis, going through the line of sight to HD 34078. The vertical and horizontal white lines corresponds to the star position. The *bottom left panel* is the integrated CO intensity.

integrated emission. They all enter in the category of diffuse clouds, i.e., $A_{\text{v}} < 1$ mag. Following Solomon et al. (1987), we yield their “virial” masses as

$$\frac{M_{\text{vir}}}{M_{\odot}} = 189 \frac{S}{1 \text{ pc}} \left(\frac{\Delta V_{\text{CO}}}{1 \text{ km s}^{-1}} \right)^2, \quad (1)$$

with S the globulette size, and ΔV_{CO} its linewidth. We also computed their luminous masses as

$$\frac{M_{\text{CO}}}{M_{\odot}} = 2 \times 1.4 \frac{m_{\text{H}}}{M_{\odot}} X_{\text{CO}} L_{\text{CO}} \quad (2)$$

with L_{CO} the globulette luminosity, m_{H} the proton mass, M_{\odot} the solar mass, and X_{CO} the standard CO-H₂ conversion factor, i.e., $2 \times 10^{20} \text{ cm}^{-2}/(\text{K km s}^{-1})$. The numerical factors account for the H₂ mass and the helium fraction. Table 3 indicates that the globulettes harbor a very small mass of molecular gas. Moreover, they are far from being gravitationally bound, since their luminous mass is at least 3 orders of magnitude smaller than their “virial” mass. However, this data alone cannot indicate whether the globulettes are currently forming, being destroyed, or in an external pressure confined equilibrium. Their large velocity dispersion $\Delta V_{\text{CO}} \approx 1-2.5 \text{ km s}^{-1}$ corresponds to an “effective” temperature of $\mu m_{\text{H}} \Delta V_{\text{CO}}^2/k = 300-1500 \text{ K}$, implying significant nonthermal support, or strong internal velocity gradients (infall, outflow, shear).

Finally, we note that the flux recovered by the PdBI dataset alone inside the central $50'' \times 50''$ field of view is only $\sim 1/3$ of the flux measured with the IRAM-30 m telescope. The recovered fraction even decreases to 1/4 when one considers the full field of view imaged at PdBI. This is not a processing artifact, as we checked that the hybrid synthesis image does recover the same total flux in the same field of view, but with such a low brightness level that it seems hidden in the interferometric noise. Thus, some faint extended emission must be present in addition to the compact structures measured by the interferometer (for a

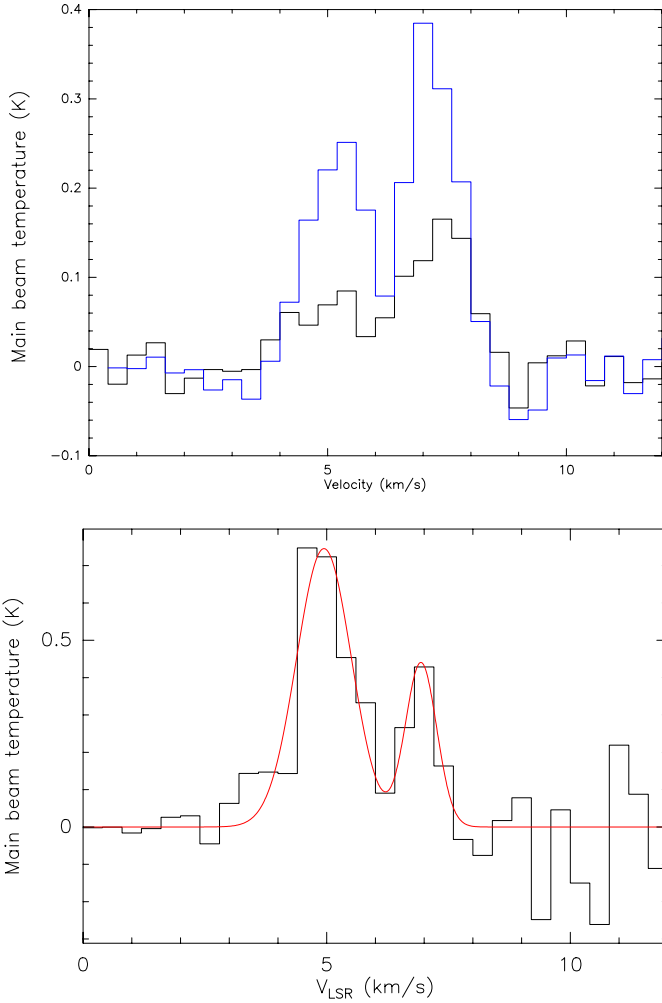


Fig. 5. Spectra observed toward the HD 34078 star. *Top:* $^{12}\text{CO}(1-0)$ (black) and $^{12}\text{CO}(2-1)$ (blue) spectra observed at the IRAM-30 m telescope. The spectra are shown at their native resolution: $21.45''$ for $^{12}\text{CO}(1-0)$ and $10.7''$ for $^{12}\text{CO}(2-1)$. *Bottom:* Hybrid synthesis $^{12}\text{CO}(1-0)$ spectrum obtained at an angular resolution of $\sim 4.4''$. The best fit, made with two gaussian components, is shown in red. The derived quantities are shown in Table 2.

detailed account of a similar effect in another context, see [Pety et al. 2013](#)). This is consistent with the fact that the deep image of the $^{12}\text{CO}(2-1)$ emission published in [Boissé et al. \(2009\)](#) shows faint emission all over the covered field of view. The low brightness structures detected here are thus probably part of a more complex extended emission that, in particular, links the bright compact emission of globulettes #1, #2, and #3. In other words, these globulettes are probably related (i.e., not distinct) entities.

4. Discussion

In this section, we first discuss how the two CO globulettes seen in the immediate vicinity of the star clarify our understanding of the peculiar properties of the line of sight toward HD 34078. We then briefly consider the possible origin and survival of these substructures. Finally, we examine the implications of our results for the nature of the IR arc and the value of the wind mass flux in HD 34078. For reference, Table 4 lists the observed and inferred parameters.

4.1. Explaining the peculiar properties of the line of sight toward HD 34078

In addition to explaining the double-peaked CO emission profiles and east-west velocity gradient seen in previous IRAM-30 m maps (see previous section), the two small CO substructures found to intercept the line of sight to HD 34078 clarify several pending issues regarding the peculiar properties of this sightline.

- *The unusually large fraction of highly excited H_2 and the high inferred gas density:* the line of sight to the star passes through the *edges* of the dense CO substructures #1 and #2, where the gas is directly exposed to the intense stellar UV flux and forms a hot photodissociation region (PDR). Such a tangent view will maximize the fraction of hot H_2 on the line of sight. At the same time, the high density in CO substructures #1 and #2 ($n_{\text{globulette}} \approx 10^5 \text{ cm}^{-3}$, see Table 3) explains the high $n_{\text{H}} \approx 0.5\text{--}5 \times 10^4 \text{ cm}^{-3}$ inferred from PDR models of the excited H_2 ([Boissé et al. 2005](#)).
- *The similar radial velocity and line width among hot and cool H_2 on the line of sight:* using a standard X_{CO} factor, the W_{CO} measured toward the star inside a $4''$ -beam (see Table 3) yields an estimated total H_2 column density of $\approx 3 \times 10^{20} \text{ cm}^{-2}$ with an uncertainty of a factor 2 (see Sect. 3). This is consistent with the column density of low-excitation H_2 at 77 K seen in absorption ($6.4 \times 10^{20} \text{ cm}^{-2}$ [Boissé et al. 2005](#)). Therefore, the cool H_2 on the line of sight also appears associated with CO substructures #1 and #2, rather than with a foreground translucent cloud unrelated to HD 34078 (as initially proposed in [Boissé et al. 2005](#)). The cool H_2 could be located preferentially on the “shadowed” side of the globulettes facing the observer, while the hot PDR would be on the irradiated side facing the star, as proposed by [Boissé et al. \(2009\)](#) in their second scenario.
- *The high abundance of CH and CH^+ :* the two components at 5 and 7 km s^{-1} in the CH and CH^+ optical absorption profiles can be unambiguously associated with CO substructures #1 and #2 (see Sect. 3). The unusually high abundance of CH and CH^+ along this line of sight ([Boissé et al. 2009](#)) might then be related to the fact that we probe a very peculiar situation. Indeed, globulettes #1 and #2 must be located close to the star, at $\approx 0.2 \text{ pc}$ ([Boissé et al. 2005](#)), to reproduce the excitation of hot H_2 on the line of sight. Interaction with the (hot) stellar wind may then be very effective in enhancing several species through turbulent mixing or shock dissipation, especially CH^+ whose formation is highly endothermic ([Boissé et al. 2009](#)).
- *The excess reddening toward HD 34078 compared to the surrounding nebula:* far-UV rocket-borne and FUSE observations of HD 34078 and its neighborhood performed by [France et al. \(2004\)](#) revealed that direct starlight is much more reddened than stellar light scattered by surrounding dust in the IC 405 nebula. This led these authors to propose the existence of an obscuring dust globulette in front of the star, with a size smaller than $\sim 20''$. Our observations provide a direct confirmation of this prediction, since substructures #1 and #2 are smaller than $10''$. The atomic gas in the hot PDR around these globulettes could contribute $\approx 1 \text{ mag}$ of extinction on the line of sight (see Table 4 of [Boissé et al. 2005](#)), i.e., a sizeable fraction of the stellar obscuration.

We stress that HD 34078 was selected for further study because of its unusually strong absorption features from dense irradiated molecular gas, as revealed, e.g., by FUSE. Therefore, the close

Table 3. Observed and inferred properties of the CO globulettes, as numbered in the right panel of Fig. 2.

#	Position (")	V_{LSR} (km s^{-1})	Size (")	ΔV_{CO} (km s^{-1})	$\langle W_{\text{CO}} \rangle$ (K km s^{-1})	$W_{\text{CO}}^{\text{peak}}$ (K km s^{-1})	$A_v^{a,b}$ (mag)	L_{CO}^c ($\text{K km s}^{-1} \text{ pc}^2$)	Mass from CO a,e (M_{\odot})	Virial Mass (M_{\odot})	$n_{\text{globulette}}^f$ (cm^{-3})
1	(−9.9, 0.3)	7.4	9.2×4.1	1.3	1.03	3.70	0.82	1.39×10^{-3}	6.21×10^{-3}	5.0	9×10^4
2	(3.8, 3.3)	5.5	10.6×5.1	2.6	1.18	2.82	0.63	1.27×10^{-3}	5.71×10^{-3}	24.1	5×10^4
3	(4.5, 13.3)	6.1	7.0×4.1	2.6^d	0.78	1.76	0.39	3.30×10^{-4}	1.48×10^{-3}	17.6	3×10^4
4	(−20.2, 24.9)	6.6	5.9×4.6	0.6	0.52	0.85	0.19	1.18×10^{-4}	5.28×10^{-4}	0.9	1×10^4
5	(29.45, 8.5)	7.3	15.2×6.8	1.1	0.46	1.06	0.24	5.04×10^{-4}	2.26×10^{-3}	6.0	1×10^4

Notes. ^(a) Computed with a standard X_{CO} conversion factor $= 2 \times 10^{20} \text{ cm}^{-2}/(\text{K km s}^{-1})$ and $N_{\text{H}}/A_v = 1.8 \times 10^{21} \text{ cm}^{-2}/\text{mag}$. ^(b) This A_v is computed from $W_{\text{CO}}^{\text{peak}}$. ^(c) Assuming a distance to HD 34078 of 530 pc, 1" corresponds to 2.6×10^{-3} pc. ^(d) The spectrum toward this globulette is double peaked, the line width estimate is an upper limit. ^(e) Including helium. ^(f) Hydrogen density computed assuming a spherical cloud with a diameter equal to the geometrical mean of the major and minor axes given in column 4 of this table.

Table 4. Parameter symbols, nominal values, and scalings in HD 34078 and its bow shock.

Definition	Symbol	Eq.	Nominal value	Scaling	Reference
Distance	D		530 pc		(1)
Spectral type	–		O9.5		(2)
Stellar mass	M_{\star}		$20 M_{\odot}$		(2)
Stellar luminosity	L_{\star}		$8 \times 10^4 L_{\odot}$	$\propto D^2$	(1)
Stellar velocity	V_{\star}		$150_{-50}^{+30} \text{ km s}^{-1}$	$\propto D$	(3)
Wind velocity	V_{wind}		800 km s^{-1}		(2)
Wind mass-loss rate (from UV)	\dot{M}		$3 \times 10^{-10} M_{\odot} \text{ yr}^{-1}$		(2)
Strömgen radius	R_{St}	(3)	4.3 pc	$\propto D$	(4)
Ambient density	n_a	(3)	20 cm^{-3}	$\propto D^{3/2}$	(4)
Wind ram pressure	P_{wind}	(4)	2300 K cm^{-3} at $R = 0.2 \text{ pc}$	$\propto \dot{M} V_{\text{wind}} R^{-2}$	(4)
Radiation pressure	P_{rad}	(8)	$1.5 \times 10^7 \text{ K cm}^{-3}$ at $R = 0.2 \text{ pc}$	$\propto D^2 R^{-2}$	(4)
Globulette thermal pressure	P_{therm}	(5)	$\sim 10^6\text{--}10^7 \text{ K cm}^{-3}$	$\propto D^{-1} T$	(4)
Star-apex distance (Observed)	R_{obs}		0.04 pc	$\propto D$	(4)
Star-apex distance (Deprojected)	R_{apex}		0.035 pc	$\propto D$	(4)
Wind standoff radius	R_{wind}	(7)	0.0012 pc	$\propto (\dot{M} V_{\text{wind}})^{1/2} D^{-7/4}$	(4)
Dust avoidance radius (no gas drag)	R_{av}	(10)	0.05–0.7 pc	$\propto D^0$	(4)
Gas+grain avoidance radius (opt. thin)	R_{rad}	(12)	$\bar{R}_{\text{av}}/100 = 0.0024 \text{ pc}$	$\propto D^0$	(4)
Gas+grain avoidance radius (opt. thick)	R'_{rad}	(13)	0.10 pc	$\propto D^{-3/4}$	(4)

Notes. References: (1) Herbig (1999); (2) Martins et al. (2005); (3) Tetzlaff et al. (2011); (4) this work.

alignment between CO substructures #1 and #2 and the line of sight seen in HD 34078 may well be the result of a selection bias. Indeed, with a transverse diameter of 4–5" and a distance to the star of 0.2 pc, these dense structures subtend an angle of only 5° as seen from the star, making such an alignment quite unlikely. This would explain why the line of sight toward HD 34078 is so peculiar.

4.2. Origin and survival of the CO globulettes on the line of sight

In order to discuss the possible origin of the small CO globulettes identified in the vicinity of HD 34078, it is important to compare their density and internal pressure to that in the surrounding H II region excited by the star. A rough estimate of the average density in the H II region may be obtained from its radius as traced by bright H α emission, which extends up to about 27 arcmin = 4.3 pc to the north of the star. Equating to the Strömgen radius (R_{St}) for an O9.5 star,

$$R_{\text{St}} \simeq 16 \left(\frac{L_{\star}}{8 \times 10^4 L_{\odot}} \right) \left(\frac{2.5 \text{ cm}^{-3}}{n_a} \right)^{2/3} \text{ pc}, \quad (3)$$

we find $n_a \sim 20 \text{ cm}^{-3}$. This estimate is only indicative as the H II region around HD 34078 is quite irregular. Thermal instability in preexisting density fluctuations could thus lead to the formation of cooler and denser filaments at 10–100 K and $10^3\text{--}10^4 \text{ cm}^{-3}$ (in pressure equilibrium with the H II region). However, this is not sufficient to reach the densities of $\approx 0.5\text{--}1 \times 10^5 \text{ cm}^{-3}$ estimated for CO globulettes #1 and #2 toward the line of sight (see Table 3). Hence, these globulettes are overpressured with respect to the surrounding H II region.

One attractive hypothesis would be that denser substructures form by compression in the bow shock driven by the stellar wind into the H II region. A bright IR arc of warm dust is indeed seen in the direction of proper motion of HD 34078 (see Fig. 1), and attributed to a stellar wind bow shock (France et al. 2007; Peri et al. 2012). Numerical simulations show that cooling instabilities will develop behind such bow shocks, creating small globulettes that are carried along the bow surface (Comeron & Kaper 1998). A hint in favor of this hypothesis is that small globulettes #3 to #5 in our map, as well as the globulette at the southeast of our field of view, all appear to lie close to the walls of a paraboloid extrapolated from the IR arc (see Fig. 2 in Sect. 2). Indeed, we show in Appendix A that the front side of this paraboloid will intercept the line of sight at 0.14 pc

from the star, for an inclination of the star motion of -30° from the plane of the sky. In addition, [Boissé et al. \(2005\)](#) showed that the highly excited H_2 on the line of sight (which we find here associated with the edges of globulettes #1 and #2) must be at an actual distance to the star of ≈ 0.2 pc. Therefore, globulettes #1 and #2, although projected close to the stellar position, also seem to lie close to the surface of the paraboloid. However, CO maps over a larger area upstream and downstream of the IR arc would be needed to confirm this correlation trend.

An important issue with such a scenario is that UV-derived stellar wind parameters from [Martins et al. \(2005\)](#) suggest a wind ram pressure at $R = 0.2$ pc from the star, which is several orders of magnitudes too low to compress CO globulettes #1 and #2 to their high observed density. Namely,

$$P_{\text{wind}}/k = \dot{M}V_{\text{wind}}/(4\pi R^2k) = 2300 \text{ K cm}^{-3}, \quad (4)$$

compared to the globulette thermal pressure

$$P_{\text{therm}}/k = n_{\text{globulette}}T \sim 10^6\text{--}10^7 \text{ K cm}^{-3} \quad (5)$$

for a plausible range of $T = 10\text{--}100$ K. Another (related) issue, pointed out by [Boissé et al. \(2009\)](#), is that the predicted wind bow shock is much too small compared to the observed size of the IR bow. Possible solutions to this problem, including a possible underestimate of the wind mass flux, are presented and discussed in the next section in the light of our new CO results.

Another process that could contribute to the compression and pressure-confinement of the globulettes is radiation-driven implosion. This eventually leads to the formation of a “cometary globule” with a photoevaporating dense head and a tail pointing away from the star (see, e.g., [Lefloch & Lazareff 1994](#)). The direction of elongation of substructures #1 and #2 is reminiscent of such a geometry. Taking their convolution by the beam size into account, their small observed transverse radius $\sim 2'' = 0.005$ pc is close to the predictions of Eq. (45) of [Lefloch & Lazareff \(1994\)](#) for a cometary globule with the observed mass $\sim 5 \times 10^{-3} M_\odot$ and linewidth $\Delta V_{\text{CO}} \approx 2 \text{ km s}^{-1}$ (corresponding to a nonthermal support with an “effective” temperature ~ 1000 K), located at 0.2 pc from an O9.5 star of total ionizing flux $S_\star = 4.7 \times 10^{47} \text{ s}^{-1}$ (for $L_\star = 8 \times 10^4 L_\odot$). Combining Eqs. (45) and (50) of [Lefloch & Lazareff \(1994\)](#), the lifetime of a cometary globule t_{CG} until complete photoevaporation may be simply expressed as a function of its radius and linewidth as

$$t_{\text{CG}} = 2.4 \times 10^4 \text{ yr} \left(\frac{R_{\text{CG}}}{0.005 \text{ pc}} \right) \sqrt{\frac{2 \text{ km s}^{-1}}{\Delta V_{\text{CO}}}}. \quad (6)$$

By that time, the star will have traveled 3.6 pc (or 0.4 deg) at a velocity of 150 km s^{-1} . Therefore, globulettes #1 and #2 seem able to survive against the harsh UV flux of the star if they are in the cometary globule phase.

4.3. Effect of radiation pressure and the weak wind problem

We now examine the implications of our results on the nature of the bright IR arc observed in the direction of propagation of HD 34078, and on the value of the wind mass flux in this star.

4.3.1. Stationary bow shock

The IR arc around HD 34078 has been traditionally attributed to a bow shock created by the stellar wind ([France et al. 2007](#); [Peri et al. 2012](#)). However, [Boissé et al. \(2009\)](#) recently questioned

this interpretation, noting that the observed star-apex distance $R_{\text{obs}} \approx 15'' = 1.2 \times 10^{17} \text{ cm} = 0.04 \text{ pc}$ was 100 times too large² compared to the expected wind standoff distance,

$$R_{\text{wind}} = \sqrt{\frac{\dot{M}V_{\text{wind}}}{4\pi\rho_a V_\star^2}} \approx 3.5 \times 10^{-4} \text{ pc} \sqrt{\frac{500 \text{ cm}^{-3}}{n_a} \left(\frac{100 \text{ km s}^{-1}}{V_\star} \right)} \quad (7)$$

if one adopts the mass-loss rate and wind velocity inferred from UV line modeling, $\dot{M} = 10^{-9.5} M_\odot \text{ yr}^{-1}$ and $V_{\text{wind}} = 800 \text{ km s}^{-1}$ ([Martins et al. 2005](#)), a stellar motion of $V_\star = 100 \text{ km s}^{-1}$, and the ambient H nucleus number density $n_a = \rho_a/(1.4m_{\text{H}}) \sim 500 \text{ cm}^{-3}$ estimated from CI and C₂ absorption lines ([Boissé et al. 2005](#); [Federman et al. 1994](#)).

Our high-resolution mapping results partly alleviate the problem noted by [Boissé et al. \(2009\)](#) since they reveal that the line of sight to the star is crossing the envelope of small dense CO globulettes, so that the density of $\sim 500 \text{ cm}^{-3}$ probed in CI and C₂ may not be representative of the large-scale ambient gas. Indeed, the size of the H II region rather suggests a mean $n_a \sim 20 \text{ cm}^{-3}$ (see Sect. 4.2), consistent with the lack of bright extended CO emission upstream of the IR arc in the IRAM-30 m data. In addition, correcting the observed star-apex distance, R_{obs} , for projection effects gives a slightly smaller true value $R_{\text{apex}} = 0.035 \text{ pc}$ (see Appendix A). At the same time, the stellar peculiar velocity has recently been constrained to $V_\star \approx 150_{-50}^{+30} \text{ km s}^{-1}$ ([Tetzlaff et al. 2011](#)). Thus, even with this lower ambient density, the predicted wind standoff radius $R_{\text{wind}} = 1\text{--}2 \times 10^{-3} \text{ pc}$ is still ~ 20 times smaller than the true star-apex distance R_{apex} .

The same issue was recently encountered in the IR bow shock driven by the runaway star ζ Oph ([Gvaramadze et al. 2012](#)), which has the same luminosity and spectral type as HD 34078. To solve this problem in the case of ζ Oph, [Gvaramadze et al. \(2012\)](#) proposed that the actual wind mass-loss rate in ζ Oph is much larger than inferred from UV lines. Indeed, there is still ongoing debate on the true wind mass fluxes in late O stars, as UV line analyses yield typically 100 times smaller values than previous H α line fitting and theoretical prescriptions – the so-called “weak-wind problem” (see, e.g., [Mokiem et al. 2007](#), for a review and possible explanations). In the case of HD 34078, we would obtain a star-apex distance $R_{\text{apex}} = 0.035 \text{ pc}$ with $\dot{M} = 1\text{--}3 \times 10^{-7} M_\odot \text{ yr}^{-1}$ for $n_a \sim 20 \text{ cm}^{-3}$ and $V_\star = 100\text{--}180 \text{ km s}^{-1}$. This is 300–1000 times larger than the UV-determined \dot{M} value, but only a few times larger than the \dot{M} inferred in ζ Oph ([Gvaramadze et al. 2012](#)), and in good agreement with the theoretical value of $2 \times 10^{-7} M_\odot \text{ yr}^{-1}$ predicted by the prescription³ of [Vink et al. \(2001\)](#) using the stellar parameters in [Martins et al. \(2005\)](#). The latter theoretical value was in fact used by [Peri et al. \(2012\)](#) to estimate the ambient density ahead of HD 34078 from the IR bow shock size (for which they adopted a slightly larger apex distance than us, of 0.06 pc). With this increased \dot{M} , the wind ram pressure at 0.2 pc would become $\approx 10^6 \text{ K cm}^{-3}$, comparable to the CO globulette thermal pressure, and may contribute to their compression at the interface. Yet, a puzzling fact in this picture is the low globulette radial velocity, which is unexpected after compression by a fast bow shock at 150 km s^{-1} .

² The star-apex distance of $1.7 \times 10^{15} \text{ cm}$ used in [France et al. \(2007\)](#) is erroneous by two orders of magnitude.

³ We could not reproduce the smaller theoretical \dot{M} quoted in [Martins et al. \(2005\)](#) for this prescription.

Boissé et al. (2009) mentioned two other effects that might help to increase the bow standoff distance without increasing \dot{M} , namely: (1) a nonstationary bow shock; (2) radiation pressure on grains. Their estimate of the ratio of radiative to wind ram pressure in HD 34078, $P_{\text{rad}}/P_{\text{wind}} \sim 10^{-3}$, was incorrect and led them to erroneously conclude that the radiation pressure was negligible, favoring option (1). The correct value $P_{\text{rad}}/P_{\text{wind}} = L_{\star}/(c\dot{M}V_{\text{wind}}) \sim 6600$, with

$$P_{\text{rad}}/k = \frac{L_{\star}}{4\pi c R^2 k} = 1.5 \times 10^7 \text{ K cm}^{-3} \quad (8)$$

suggests that radiation pressure may actually have a significant effect. Given the importance of determining accurate wind mass fluxes in late O stars such as HD 34078, we thus reexamine and quantify both options to see whether they may explain the large observed star-apex distance, as well as the apparent good correlation of the IR arc with the CO globulettes, while conserving the UV-determined \dot{M} value.

4.3.2. Nonstationary bow shock

In this scenario, we would be witnessing a transient situation where the bow shock was initially propagating into a very low density medium at $n_a \leq 0.02 \text{ cm}^{-3}$ (so that $R_{\text{wind}} \geq 0.04 \text{ pc}$), and is just now entering a much denser region to the north at 10 cm^{-3} . The wind ram pressure at the interface would now be much smaller than the ambient pressure, so that the apex is essentially stalled at its current position. It will remain so until the star-apex distance has decreased to a few times its new equilibrium standoff value 10^{-3} pc . The needed time is thus approximately the time for the star to propagate over 0.04 pc , i.e., 260 yr at 150 km s^{-1} . This is so short that it seems very unlikely. It appears even more implausible to believe that $\zeta \text{ Oph}$ could also be caught in the same transitory situation.

4.3.3. Radiation pressure on dust grains without gas drag

Artymowicz & Clampin (1997) described the trajectory of dust grains *without gas drag* near a bright moving star and showed that the dust grains are repelled outside of an avoidance region with a paraboloidal shape focused at the star. The standoff avoidance radius of the parabola for a grain of radius s is given by

$$R_{\text{av}}(s) = 2 [\beta(s) - 1] \frac{GM_{\star}}{V_{\star}^2}, \quad (9)$$

where $\beta(s) \propto L_{\star}/M_{\star}$ is the ratio of radiation pressure to gravity for that grain (see Eq. (4) in Artymowicz & Clampin 1997). For an O star, $\beta(s) \gg 1$ (negligible gravity) and the dependences on M_{\star} in β and R_{av} cancel out, so that

$$R_{\text{av}}(s) = 0.24 \text{ pc} \left(\frac{L_{\star}}{8 \times 10^4 L_{\odot}} \right) \left(\frac{150 \text{ km s}^{-1}}{V_{\star}} \right)^2 \times \left(\frac{Q_{\text{pr}}(s)/s}{30 \mu\text{m}^{-1}} \right) \left(\frac{2.2 \text{ g cm}^{-3}}{\rho_{\text{bulk}}} \right). \quad (10)$$

The adopted value of ρ_{bulk} is for a 50%-50% compact mixture of astronomical silicates and graphite (Artymowicz & Clampin 1997). The Planck-averaged value of $Q_{\text{pr}}(s)/s$ for an incident blackbody at $T_{\star} = 31 \text{ 000 K}$ (appropriate for an O9.5 star) varies strongly with grain radius, from ≈ 85 at small radii $s \leq 0.01 \mu\text{m}$ to ≈ 6 at $s = 0.3 \mu\text{m}$ (Laor & Draine 1993). Hence, the dust avoidance radius $R_{\text{av}}(s)$ also varies strongly over this size range,

from 0.7 to 0.05 pc . Modeled IR images taking into account the variation of $\beta(s)$ over grain size for an MRN distribution are presented by Gáspár et al. (2008) and show a broadening of the IR arc that seems consistent with the $24 \mu\text{m}$ *Spitzer* image in HD 34078. The value of $Q_{\text{pr}}(s)/s = 30$ in the above scaling is a mass-weighted average over a standard MRN size distribution with $n(s) \propto s^{-3.5}$ in the range $[0.005 \mu\text{m}, 0.25 \mu\text{m}]$, and corresponds to a grain of size $\bar{s} = 0.05 \mu\text{m}$. The corresponding mass-weighted avoidance radius, $\overline{R_{\text{av}}} = 0.24 \text{ pc}$ is a factor 7 larger than the star-apex distance of the IR arc in HD 34078. Given the relative uncertainty in V_{\star} (a factor 1.5) and in dust properties (composition, size distribution, volume density, and porosity), this might still be considered a promising agreement⁴.

A strong caveat of this model is that it cannot explain the distortion of the IR arc observed in the $24 \mu\text{m}$ image from a perfect paraboloidal shape pointing in the direction of motion of the star (Fig. 1 shows that the eastern and western wings of the arc are better reproduced with a different R_{obs} , of $20''$ and $10''$, respectively). Indeed, unlike the wind standoff radius R_{wind} , the dust avoidance radius R_{av} in Eq. (10) is *independent of the ambient density* so that a parabola aligned with V_{\star} should result, whatever the inhomogeneities present in the medium ahead of the star. Another issue is that the IR bow shock distance in runaway stars of similar spectral types and dust properties should vary as $R_{\text{av}} \propto L_{\star}/V_{\star}^2$, regardless of ambient density. This relation predicts that the IR bow shock in the O9.5 star $\zeta \text{ Oph}$, where $L_{\star} \approx 6 \times 10^4 L_{\odot}$ and $V_{\star} \approx 25 \text{ km s}^{-1}$ (Gvaramadze et al. 2012), should be 12–40 times larger than in HD 34078 (where $L_{\star} = 8 \times 10^4 L_{\odot}$ and $V_{\star} = 100\text{--}180 \text{ km s}^{-1}$), whereas one observes only a factor 4.

The above determination of R_{av} assumes negligible gas drag, i.e., that grains and gas are totally decoupled. Therefore, the gas will continue to approach the star until it meets the wind bow shock defined by the (tiny) value of $R_{\text{wind}} \approx 10^{-3} \text{ pc}$ for the UV-determined \dot{M} . The fact that the CO globulettes in our maps appear to lie on the same surface as the dust avoidance parabola defined by the IR arc might then be understood if they quickly photodissociate when entering the avoidance region, as they leave the dust behind. However, the density in the CO globulettes appears too high for dust and gas to remain decoupled. The distance $d(s)$ over which a grain of radius s and bulk density ρ_d will sweep up its own mass in gas is

$$d(s) = 0.04 \text{ pc} \left(\frac{100 \text{ cm}^{-3}}{n_a} \right) \left(\frac{s}{0.1 \mu\text{m}} \right) \left(\frac{\rho_d}{2.23 \text{ g cm}^{-3}} \right). \quad (11)$$

We thus expect significant dust-grain coupling to occur on observed scales if the density exceeds a few 100 cm^{-3} , which is certainly the case inside the dense CO globulettes even for the largest grains.

4.3.4. Radiation pressure on dust grains with gas drag (optically thin case)

We now consider how the avoidance radius created by radiation pressure on grains would change in the presence of gas drag. In the limiting case of perfect gas-grain coupling, the radiation pressure force on grains (assumed optically thin to the stellar radiation) will be entirely transferred to the gas. As demonstrated in Appendix B, the dynamics of the coupled fluid upstream of

⁴ As the motion of H34078 is mainly in the plane of the sky, V_{\star} is to first order $\propto D$. Furthermore, L_{\star} is $\propto D^2$ for a given apparent magnitude, reddening, and spectral type. Therefore $R_{\text{av}}(s) \propto L_{\star}/V_{\star}^2$ is independent of the assumed distance.

the avoidance radius remains similar to the dynamics for pure dust grains, except that the effective ratio of pressure to gravity $\bar{\beta}$ (averaged over the grain size distribution) is divided by the gas-to-dust ratio (ρ_g/ρ_d) ≈ 100 because of the gas inertia. The resulting standoff radius is given by the mass-weighted dust avoidance radius \bar{R}_{av} reduced by the same factor of 100, i.e.,

$$R_{rad} \approx 2.4 \times 10^{-3} \text{ pc} \quad (12)$$

for the parameters of HD 34078. Unlike pure dust grains, the dusty gas will not “bounce” off the avoidance parabola, but undergo a shock front and slide along the parabola walls. The additional wind ram pressure acting on the fluid will increase this shock standoff distance to a value close to the maximum between R_{rad} and R_{wind} (see Appendix B).

The relative importance of radiation pressure versus wind ram pressure in defining the standoff radius in this (optically thin) case is quantified by the ratio R_{rad}/R_{wind} , rather than by the ratio P_{rad}/P_{wind} . Since R_{rad} is even smaller than R_{wind} for the standard value of \dot{M} , radiation pressure on grains in the dense CO globulettes (assumed optically thin) does not explain, alone, their observed distribution along the IR arc, which has a standoff distance 15 times larger⁵.

4.3.5. Radiation pressure on dust grains with gas drag (optically thick case)

The situation may change if the dense globulettes with good gas-grain coupling become optically thick to stellar UV radiation. We note that the maximum effect will be obtained by replacing P_{wind} by P_{rad} in the expression of R_{wind} , i.e., in Eq. (7). Such an upper limit would be reached if the incoming globulettes do not feel the radiation pressure of the star until they get to the bow shock, because of the screening by other optically thick globulettes closer to the bow surface. For the parameters of HD 34078 and $V_\star = 150 \text{ km s}^{-1}$, this would give

$$R'_{rad} = R_{wind} \sqrt{(P_{rad}/P_{wind})} \approx 0.1 \text{ pc}. \quad (13)$$

The similarity with the value of \bar{R}_{av} is purely coincidental, since the dependence on stellar parameters and ambient density is different, with $R'_{rad} \propto \sqrt{L_\star/n_a} \times (1/V_\star)$. Such a scaling would better explain the ratio of 4 between the IR apex size in ζ Oph and HD 34078, if the ambient densities are similar. And the dependence on n_a could explain bow shock distortions with a density (or magnetic pressure) gradient inclined with respect to the star’s proper motion, in contrast to the case of pure dust avoidance. However, the assumption of an optically thick bow shock is clearly too extreme as the star is able to ionise a large H II region ahead of it. A more realistic modeling is outside the scope of the present paper, but would be useful.

5. Conclusions

We described the calibration and construction of the ^{12}CO (1–0) imaging at $\sim 10^{-3} \text{ pc}$ ($\sim 4.4''$) of the $\sim 0.31 \times 0.26 \text{ pc}$ ($\sim 120'' \times 100''$) toward the runaway O star HD 34078, using observations

⁵ In a paper accepted while this work was under revision, Ochsendorff et al. (2014) investigate the case of imperfect gas-drag and argue that it could explain the IR arc sizes in runaway stars such as σ Ori and ζ Oph if grains in H II regions are much less charged than usually assumed. Like us, however, they still predict too small a size for the infrared arc in HD 34078 where V_\star is large and gas-grain drag is dominated by direct collisions rather than by coulomb interactions.

from both the PdBI and IRAM-30 m telescopes. The IRAM-30 m data mainly features two unresolved globules: one at the southeastern edge of the observed field of view, not discussed here, and a second one around the star sightline. At the PdBI resolution, the latter appears to be composed mainly of two bright (1 and 3 K peak temperature) and compact (size $\leq 10''$ or 0.026 pc) globulettes linked together by an extended faint emission that amounts to two-thirds of the total flux.

The star sightline clearly intercepts the edge of globulette #2. However, the spectrum in the direction of the star is double-peaked, indicating that the star sightline also intercepts globulette #1. These globulettes are responsible for the absorption lines from CH, CH⁺, and cold H₂ at 77 K, and also explain the large amounts of dense excited H₂ at 350 K on this sightline, the latter probably tracing a PDR on the illuminated face of the globulettes. The measured CO column density in this direction is compatible with the stellar reddening measured in the far-UV and visible. The globulettes are small enough for the surrounding reflexion nebula to be less reddened than the star (France et al. 2007). The imaged CO globulettes appear to approximately lie along the parabola walls. They are clearly not gravitationally bound. They may be pressure confined and they probably result from the interaction between the star and the preexisting diffuse gas (e.g., thermal instabilities in the bow shock).

We quantified the actions of two competing processes in the interaction between the star and the preexisting diffuse nebula, IC 405. The first one is ram-pressure due to the high velocity star wind. The second one is the radiative pressure (optically thin case) on the dust grains that entrain the gas through friction.

Neither a nonstationary bow shock nor the effect of radiation pressure (in the optically thin limit) can simultaneously explain (1) the observed large size of the IR arc in HD 34078; (2) its distortion from a perfect parabolic shape; (3) its size ratio of 4 compared to that around ζ Oph; and (4) its spatial correlation with dense CO globulettes. The most straightforward explanation for these four properties appears to be that the wind mass flux is 300–1000 times larger than indicated by UV lines, and close to the theoretical prescription of Vink et al. (2001). The effect of radiation pressure on optically thick globulettes would be important to investigate, but may also prove insufficient. Indeed, the low radial velocities observed in the CO globulettes appear puzzling for a steady-state wind bow shock.

A study over a wider field of view in both CO and H α , including regions both upstream and downstream from the IR arc, would be important to obtain additional constraints on the formation process and dynamical state of the CO globulettes.

Acknowledgements. This work has been funded by the grant ANR-09-BLAN-0231-01 from the French Agence Nationale de la Recherche as part of the SCHISM project (<http://schism.ens.fr/>). P.G. acknowledges support from the ERC Starting Grant (3DICE, grant agreement 336474) at the end of this work. J.P. and P.G. thanks H.S. Liszt, R. Lucas, and A. Witt for their encouragement during this work.

Appendix A: Projection effects

Projections effects must be taken into account when interpreting the observed contours of the paraboloid because the star velocity vector V_\star lies out of the plane of the sky. Let i be the inclination of the velocity vector with respect to the plane of the sky, with $i < 0$ when the star is receding. In our case, $i \approx -30^\circ$. Figure A.1.a shows the natural reference frame, named $Oxyz$, associated with the star motion: O coincides with the star position, Oy is parallel to V_\star , and Ox is in the plane of the sky. Adopting the star-apex

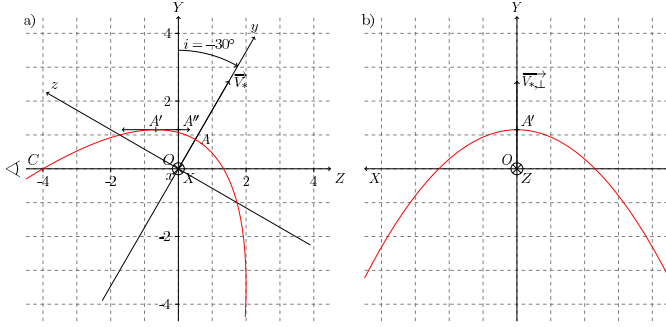


Fig. A.1. Projections of a paraboloid shape from the natural star frame to the observer frame. Panel **a)** shows a cut through the paraboloid in the plane $x = X = 0$ defined by the star proper motion vector \mathbf{V}_* and the line of sight (Z axis pointing away from the observer). Point A is the real apex of the parabola, A' is the apparent apex as seen by the observer, A'' the projection of A' on the Y axis, and C the intersection of the front side of the parabola with the line of sight. Panel **b)** shows the paraboloid apparent shape as seen in projection in the XY plane of the sky.

distance OA as unit length, the equation of the paraboloid in this frame is $y = 1 - (x^2 + z^2)/4$.

The observer frame, named $OXYZ$, is rotated by $-i$ about $Ox = OX$ so that OZ is pointing away from the observer, and OY is the projection of \mathbf{V}_* in the plane of the sky. For $i \neq 0$, the equation of the paraboloid in the $OXYZ$ frame can be obtained by performing the appropriate coordinate rotation. This yields

$$-Z \sin i + Y \cos i = 1 - \frac{(Z \cos i + Y \sin i)^2 + X^2}{4}. \quad (\text{A.1})$$

This allows us to define the coordinates of three specific points of the parabola. The apparent apex A' is the point in the $X = 0$ plane where $dY/dZ = 0$. We obtain $Z = \sin i / \cos^2 i$ and the apparent star-apex distance $Y_{\max} = 1 / \cos i$. The two points of the parabola intersecting the line of sight are found by setting $Y = 0$ and $X = 0$ in Eq. (A.1). The two solutions are

$$Z_{\pm} = \frac{2 \sin(i \pm 2)}{\cos^2 i} = \frac{2 \sin(i \pm 2)}{\cos i} Y_{\max}. \quad (\text{A.2})$$

Figure A.1b shows the shape of the paraboloid as seen in projection in the plane of the sky. It is obtained by setting $dX/dZ = 0$ in Eq. (A.1). This yields

$$Y \cos i = 1 - \frac{X^2 \cos^2 i}{4}. \quad (\text{A.3})$$

This still is a parabola focused in O . This curve intersects the X -axis at a projected distance from the star $X = \pm 2 / \cos i = \pm 2 Y_{\max}$. The projected parabola thus has an aspect ratio identical to the original one.

For $i = -30^\circ$ and an observed star-apex distance of $OA'' = 0.04$ pc, we infer the true star-apex distance $OA = OA'' \cos i = 0.035$ pc. The distance from the star to the intersection point C closest to the observer is then $OC = 2OA'' (\sin i - 1) / \cos i = 0.14$ pc.

Appendix B: Radiation pressure on grains with gas-drag

The dust-gas collisions exchange momentum between the gas and dust components and thus transfer the radiative impulsion

felt by the grains to the gas. The dust momentum equation reads

$$D_t(\rho_d \mathbf{V}_d) = (\bar{\beta} - 1) \frac{GM_\star}{R^3} \hat{\mathbf{R}} \rho_d + \mathbf{F}_d, \quad (\text{B.1})$$

where D_t denotes the Lagrangian derivative $\partial_t + \mathbf{V} \cdot \nabla$, \mathbf{V}_d and ρ_d are the dust velocity and density per unit volume of gas, R is the distance from the star with its unit vector $\hat{\mathbf{R}}$, $\bar{\beta}$ is the ratio between the radiative force on the grains and the gravitational force (cf. Artymowicz & Clampin 1997) averaged over the grain size distribution, and \mathbf{F}_d is the momentum transfer between gas and dust due to dust-gas friction. The corresponding equation for the gas fluid is

$$D_t(\rho_g \mathbf{V}_g) + \nabla p = -\frac{GM_\star}{R^3} \hat{\mathbf{R}} \rho_g - \mathbf{F}_d, \quad (\text{B.2})$$

with ρ_g and \mathbf{V}_g the gas mass density and velocity, and p the thermal pressure. If we sum up these two equations to get the evolution for the total momentum, we get

$$D_t(\rho_g \mathbf{V}_g) + D_t(\rho_d \mathbf{V}_d) + \nabla p = (\bar{\beta} \rho_d - \rho_g - \rho_d) \frac{GM_\star}{R^3} \hat{\mathbf{R}}. \quad (\text{B.3})$$

We now assume 1) that the gas ram pressure dominates both its thermal pressure p and the ram pressure of the dust; 2) that the system has reached a steady-state with $\partial_t \equiv 0$; 3) that we are on the star-apex axis, an axis of symmetry for the system; and 4) that $\partial_x(\mathbf{V}_g)_x \simeq 0$ where x is any direction orthogonal to the star-apex axis (i.e., the slight divergence of the incoming flow is negligible at the apex). The total momentum equation then yields

$$\partial_R(\rho_g V_g^2) = \alpha \frac{GM_\star}{R^2} \rho_g, \quad (\text{B.4})$$

where $\alpha = \bar{\beta} \rho_d / \rho_g - 1$. Similarly, the continuity equation yields

$$\partial_R(\rho_g V_g) = 0. \quad (\text{B.5})$$

Under these approximations, the gas behaves exactly like dust with an effective $\bar{\beta}$ lowered by the factor ρ_d / ρ_g . We use ρ_a and V_\star as the corresponding values of ρ_g and V_g far from the star. The above conservation Eqs. (B.4) and (B.5) become

$$\rho_g V_g = \rho_a V_\star \quad (\text{B.6})$$

$$\text{and } \frac{1}{2} V_g^2 + \alpha \frac{GM_\star}{R} = \frac{1}{2} V_\star^2, \quad (\text{B.7})$$

which completely constrain the profile of the gas mass density and velocity in the upstream gas under the repulsive effect of radiation pressure. We define $R_{\text{rad}} = 2\alpha GM_\star / V_\star^2$ the corresponding “hybrid” gas+grain avoidance radius where $V_g = V_d = 0$ in the presence of grain-gas coupling.

We then look for the corresponding steady-state stand-off radius R_{apex} of the bow shock created by the stellar wind. Its position is determined by the balance (in the reference frame of the star) between the ram pressures in the wind and in the incoming gas stream

$$\rho_w V_{\text{wind}}^2 = \rho_g V_g^2. \quad (\text{B.8})$$

We denote as R_{wind} the wind stand-off radius in the absence of dust drag, i.e., when $V_g = V_\star$. The radiation pressure on dust lowers the velocity of the upstream gas to $V_g < V_\star$, hence the pressure balance will be obtained for $R_{\text{apex}} > R_{\text{wind}}$. Similarly, if $V_{\text{wind}} > 0$, the ram pressure balance will occur at $V_g > 0$, hence

$R_{\text{apex}} > R_{\text{rad}}$. Thus, R_{apex} will be larger than both R_{wind} and R_{rad} . Combining Eqs. (B.6)–(B.8), we obtain

$$\left(\frac{R_{\text{wind}}}{R_{\text{apex}}}\right)^2 = \sqrt{1 - \frac{R_{\text{rad}}}{R_{\text{apex}}}}. \quad (\text{B.9})$$

Finally, with $x = R_{\text{wind}}/R_{\text{apex}}$, this last equation becomes

$$x^4 + \frac{R_{\text{rad}}}{R_{\text{wind}}}x - 1 = 0, \quad (\text{B.10})$$

which completely determines R_{apex} from R_{rad} and R_{wind} .

The stand-off radius is only slightly larger than the largest value between R_{rad} and R_{wind} . When $R_{\text{wind}} \gg R_{\text{rad}}$, the gas feels almost no dust drag due to radiation pressure before entering the shock and $R_{\text{apex}} \simeq R_{\text{wind}}$. Conversely, when $R_{\text{rad}} \gg R_{\text{wind}}$, the wind ram pressure is quickly negligible ahead of the avoidance radius and $R_{\text{apex}} \simeq R_{\text{rad}}$. When $R_{\text{wind}} = R_{\text{rad}}$, we have $R_{\text{apex}} \simeq 1.5R_{\text{wind}}$.

References

- Artymowicz, P., & Clampin, M. 1997, *ApJ*, 490, 863
 Bagnuolo, Jr., W. G., Riddle, R. L., Gies, D. R., & Barry, D. J. 2001, *ApJ*, 554, 362
 Blaauw, A., & Morgan, W. W. 1953, *Bull. Astron. Inst. Netherlands*, 12, 76
 Boissé, P., Le Petit, F., Rollinde, E., et al. 2005, *A&A*, 429, 509
 Boissé, P., Rollinde, E., Hily-Blant, P., et al. 2009, *A&A*, 501, 221
 Comeron, F., & Kaper, L. 1998, *A&A*, 338, 273
 Federman, S. R., Strom, C. J., Lambert, D. L., et al. 1994, *ApJ*, 424, 772
 Fitzpatrick, E. L., & Massa, D. 1990, *ApJS*, 72, 163
 France, K., McCandliss, S. R., Burgh, E. B., & Feldman, P. D. 2004, *ApJ*, 616, 257
 France, K., McCandliss, S. R., & Lupu, R. E. 2007, *ApJ*, 655, 920
 Gáspár, A., Su, K. Y. L., Rieke, G. H., et al. 2008, *ApJ*, 672, 974
 Gvaramadze, V. V., Langer, N., & Mackey, J. 2012, *MNRAS*, 427, L50
 Herbig, G. H. 1958, *PASP*, 70, 468
 Herbig, G. H. 1999, *PASP*, 111, 809
 Laor, A., & Draine, B. T. 1993, *ApJ*, 402, 441
 Lefloch, B., & Lazareff, B. 1994, *A&A*, 289, 559
 Martins, F., Schaerer, D., Hillier, D. J., et al. 2005, *A&A*, 441, 735
 Mokiem, M. R., de Koter, A., Vink, J. S., et al. 2007, *A&A*, 473, 603
 Ochsendorf, B. B., Cox, N. L. J., Krijt, S., et al. 2014, *A&A*, 563, A65
 Peri, C. S., Benaglia, P., Brookes, D. P., Stevens, I. R., & Isequilla, N. L. 2012, *A&A*, 538, A108
 Pety, J., & Rodríguez-Fernández, N. 2010, *A&A*, 517, A12
 Pety, J., Schinnerer, E., Leroy, A. K., et al. 2013, *ApJ*, 779, 43
 Rodríguez-Fernández, N. J., Pety, J., & Gueth, F. 2008, *Tech. Rep. 2008-2, IRAM*
 Rollinde, E., Boissé, P., Federman, S. R., & Pan, K. 2003, *A&A*, 401, 215
 Shull, J. M., & van Steenberg, M. E. 1985, *ApJ*, 294, 599
 Solomon, P. M., Rivolo, A. R., Barrett, J., & Yahil, A. 1987, *ApJ*, 319, 730
 Tetzlaff, N., Neuhäuser, R., & Hohle, M. M. 2011, *MNRAS*, 410, 190
 Vink, J. S., de Koter, A., & Lamers, H. J. G. L. M. 2001, *A&A*, 369, 574
 Wilkin, F. P. 1996, *ApJ*, 459, L31